

Atomic Fe–N Doped Multi-Cavity Hollow Carbon Nanoreactor as an Efficient Electrocatalyst for Lithium-Sulfur Batteries

Haodong Shi,^[a] Panpan Su,^[a] Cong Dong,^[a, b] Jian Liu,^{*[a, c]} and Zhong-Shuai Wu^{*[a, c]}

Lithium-sulfur (Li–S) batteries have been highly praised for the key rechargeable batteries due to their numerous advantages. However, the sluggish conversion and shuttling effect of polysulfides restrict their practicality. Here we rationally design the multi-cavity hollow carbon spheres doped with atomic Fe–N sites (Fe–N/MCHCS) as physically/chemically double-confined catalytic nanoreactors for the efficient sulfur host materials. The Fe–N/MCHCS with hierarchical porous structure and high pore volume ensures the high loading mass, and the multi-cavity structures significantly buffer the volume expansion of sulfur and enhance the electronic contact. Meanwhile, atomic

Fe offers chemical binding site and efficiently catalyzes the conversion of polysulfides during cycling, thus immobilizing and alleviating the shuttling effect of polysulfides. Consequently, the Fe–N/MCHCS nanoreactor based Li–S batteries deliver a long cycling life of 1135 mAh g⁻¹ after 300 cycles at 0.5 C and high-rate capability of 1055 mAh g⁻¹ at 8 C. Even under practical conditions with a high sulfur mass loading of 5.0 mg cm⁻², a steady areal capacity of 4.85 mAh cm⁻² is attained. This strategy combining multi-cavity hollow carbon with single atom catalysis opens a reliable route to design highly stable and high-performance Li–S batteries.

Introduction

Li–S batteries with the merits of high theoretic specific energy (2567 Wh kg⁻¹) and environmental friendliness are one kind of promising new-generation of rechargeable batteries.^[1] Furthermore, sulfur as the cathode of Li–S batteries, is earth abundant and low cost.^[2] However, the two issues arises from the low electrical conductivity of sulfur and the dissolution of lithium polysulfides usually lead to poor cyclability of Li–S batteries.^[3] During charging-discharging process, large volume expansion of the cathode can even result in the collapse of electrodes.^[4] The above challenging issues substantially restrict the commercialization of Li–S batteries.

In order to address the above problems, carbon materials as host have been widely investigated, which can effectively improve the loading amount, conductivity and utilization of sulfur.^[5] The porous structures including pore size and pore volume of carbon are pivotal for the performance of Li–S

batteries.^[6] In the last decade, various carbon materials including mesoporous carbon and hollow carbon spheres have been applied as the sulfur hosts.^[7] Among them, hollow carbon spheres with the large cavity exhibit the high sulfur loading amount, while limited contact area of sulfur with host in hollow carbon spheres blocks the effective utilization of sulfur.^[8] Although the desired porous structures are expected to confine lithium polysulfides to prohibit its dissolution, the weak interaction between carbon host and lithium polysulfide via this physical confinement is very limited.

Distinct from the physical confinement of carbon host, metal sulfides can interact with lithium polysulfides via chemical bonds, which exhibit the strong chemical confinement and effectively prohibit the diffusion of lithium polysulfides.^[9] While the low specific surface area and limited pore structures of metal-based compositions lead to the low sulfur loading. Besides of metal-based compositions, single-atom metal catalysts, such as Zn–N/C, V–N–C, Ni–N–C and Co–N–C can effectively catalyze the formation and decomposition of lithium polysulfides.^[10] Taking the sulfur loading amount and effective confinement of lithium polysulfides into consideration, doping the highly active single-atom metal catalysts into carbon hosts with desired porous structure is an effective solution to achieve the excellent performance of Li–S batteries.

Herein, we designed a new class of multi-cavity hollow carbon spheres doped with atomic Fe–N sites (Fe–N/MCHCS) as a physically/chemically double-confined nanoreactor for boosting Li–S batteries. The Fe–N/MCHCS with highly dispersed atomic Fe possesses hierarchical porous structure, high conductivity, large pore volume and specific surface area, providing highly effective chemical adsorption, physical confinement and catalytic conversion for lithium polysulfides. As a consequence, the diffusion of polysulfides is successfully suppressed and the

[a] Dr. H. Shi, Dr. P. Su, C. Dong, Prof. J. Liu, Prof. Z.-S. Wu
State Key Laboratory of Catalysis
Dalian Institute of Chemical Physics, Chinese Academy of Sciences
457 Zhongshan Road, Dalian 116023, China
E-mail: jianliu@dicp.ac.cn
wuzs@dicp.ac.cn

[b] C. Dong
University of Chinese Academy of Sciences
19 A Yuquan Rd, Shijingshan District, Beijing 100049, China

[c] Prof. J. Liu, Prof. Z.-S. Wu
Dalian National Laboratory for Clean Energy
Chinese Academy of Sciences
457 Zhongshan Road, Dalian 116023, China

 Supporting information for this article is available on the WWW under
<https://doi.org/10.1002/batt.202200154>

 An invited contribution to a Special Collection on IV Symposium on Advanced Energy Storage.

reactivity of sulfur is greatly activated. When applied in Li–S batteries, the Fe–N/MCHCS–S cathode exhibits outstanding electrochemical performance, including a high reversible capacity of 1135 mAh g^{-1} after 300 cycles with coulombic efficiency of nearly 100% at 0.5 C, an unprecedented rate capacity of 1055 mAh g^{-1} is reached even under high rate of 8 C. More crucially, the designed multi-cavity structures also achieve a remarkable areal capacity of 4.85 mAh cm^{-2} at 5.0 mg cm^{-2} , showing the great potential for practical applications.

Results and Discussion

Synthesis and characterization of Fe–N/MCHCS

The synthetic process of Fe–N/MCHCS is shown in Figure 1(a). Firstly, dopamine hydrochloride was polymerized around hollow mesoporous silica spheres (HMSS, Figure S1), and then carbonized followed by etching with hydrofluoric acid to remove HMSS core and get nitrogen doped multi-cavity hollow carbon spheres

(N/MCHCS). Finally, atomic iron was uniformly anchored on N/MCHCS to form Fe–N/MCHCS via chemical coordination with nitrogen species.

To characterize the morphologies and microstructures of the prepared materials, scanning electron microscopy (SEM, Figure S2) and transmission electron microscopy (TEM) were firstly adopted. Figure 1(b) shows several large through-holes distributed on the shell of HMSS. Using this HMSS as templates, the as-prepared N/MCHCS and Fe–N/MCHCS show double-shell structure which contains several to ten cavities (Figure 1c, d). The distance between double shell is decreased to 85 nm for Fe–N/MCHCS from 100 nm for N/MCHCS, which is contributed to the structure shrink induced by thermal treatment during atomic Fe modification. High-angle annular dark field (HADDF)-scanning tunneling microscopy (STEM) images was performed. Figure 1(e) reveals the uniform distribution of elemental C, N, O and Fe in Fe–N/MCHCS, and individual atomic Fe (bright dots signalized by red circles) are observed on the support as shown in Figure 1(f). XRD pattern of Fe–N/MCHCS shows only the diffraction peak of carbon (Figure 2a), which indicates the

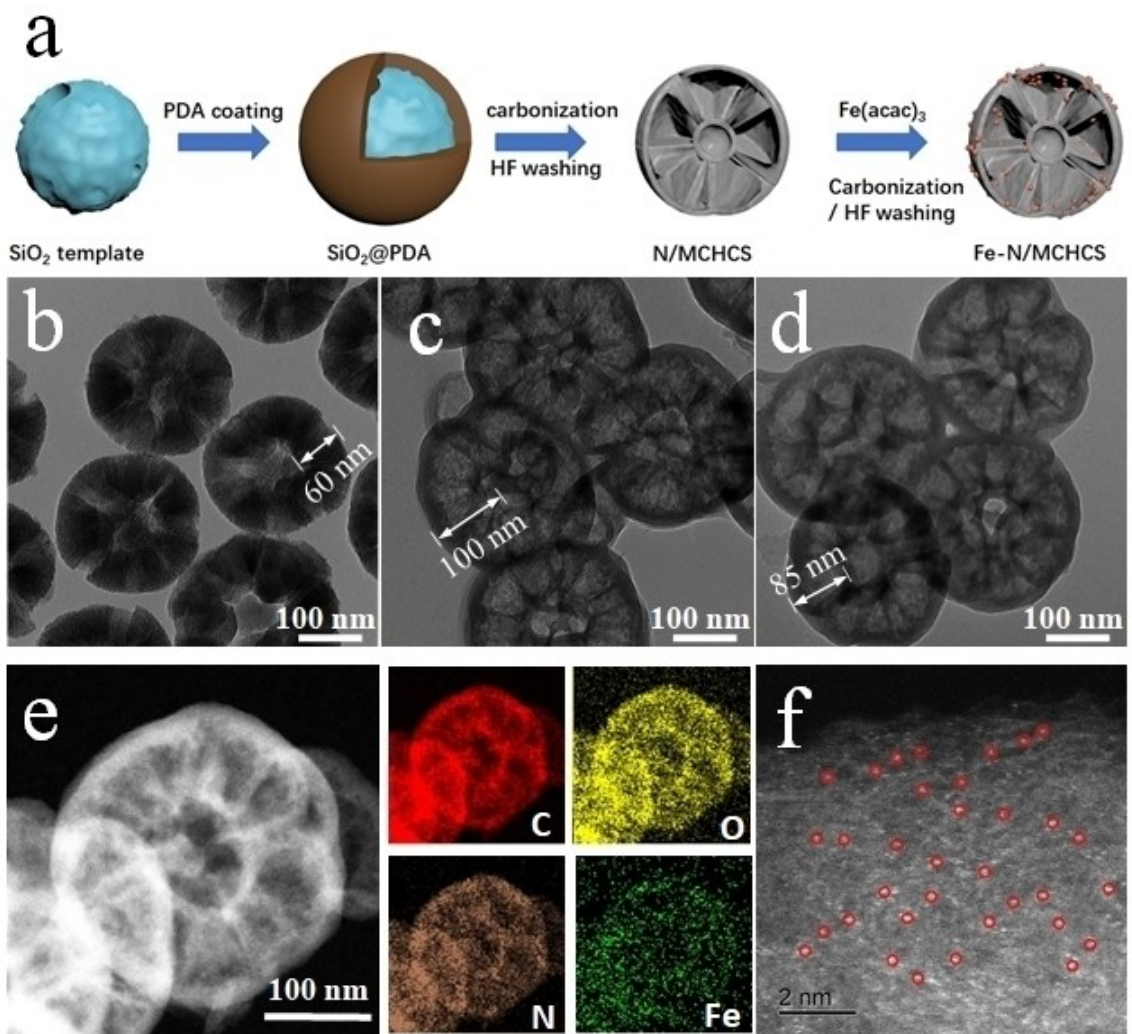


Figure 1. a) The synthetic process of Fe–N/MCHCS. b–d) TEM images of (b) HMSS template, c) N/MCHCS and d) Fe–N/MCHCS. e) Elemental mapping of C (red), O (yellow), N (orange), Fe (green) and f) HAADF-STEM image of Fe–N/MCHCS.

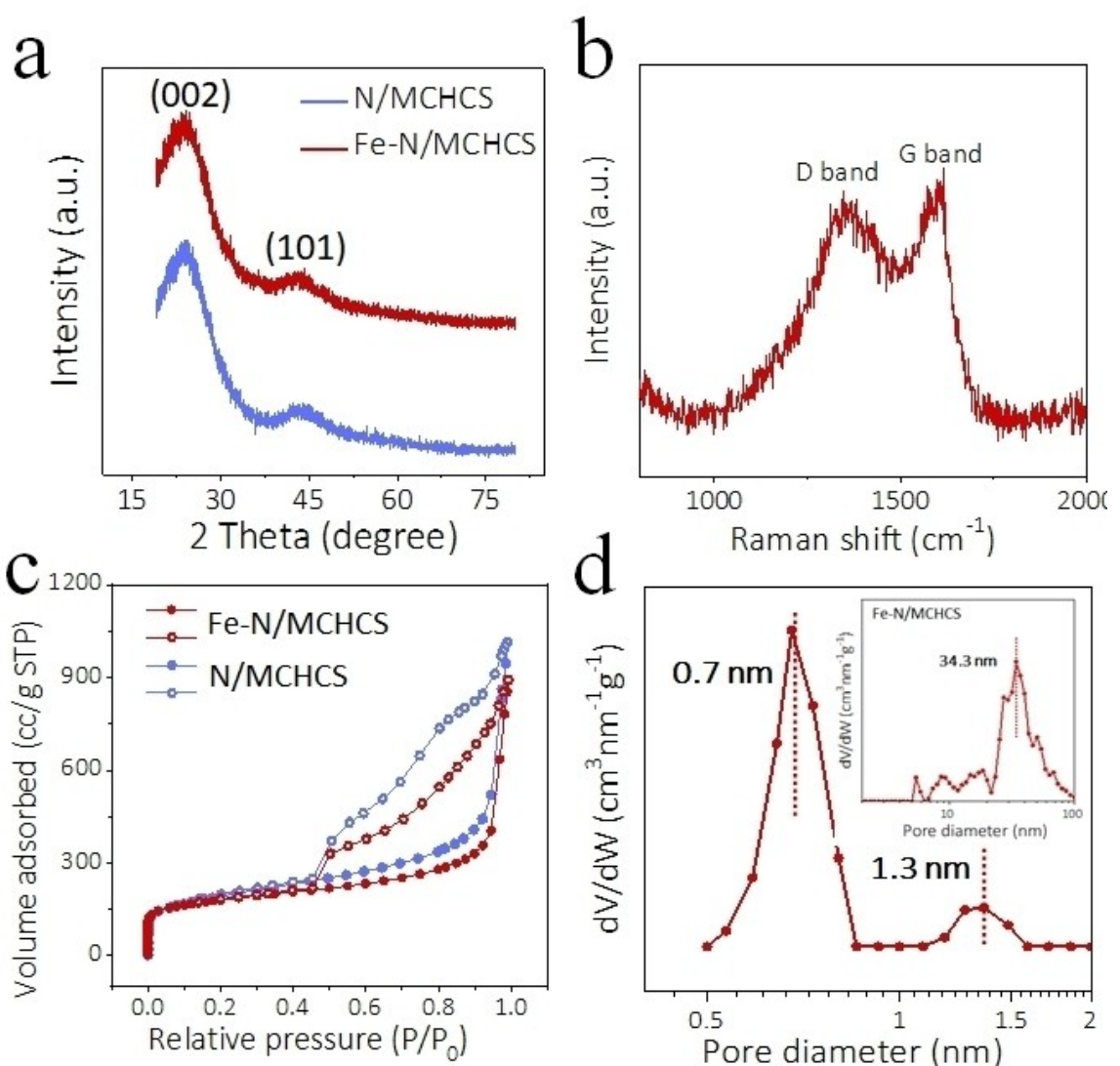


Figure 2. a) XRD patterns of N/MCHCS and Fe–N/MCHCS. b) Raman spectrum of Fe–N/MCHCS. c) The nitrogen adsorption-desorption isotherms for N/MCHCS and Fe–N/MCHCS, and d) pore size distribution curves of Fe–N/MCHCS.

absence of Fe particles and consistent with HAADF-STEM image. Raman spectrum was also carried out for this sample. The D (1355 cm^{-1}) and G (1598 cm^{-1}) bands originated from the disordered carbon induced by sp^3 defects and ordered graphitic carbon layer (sp^2), respectively (Figure 2b). The low intensity ratio ($I_{\text{D}}/I_{\text{G}}$) 0.93 suggests that Fe–N/MCHCS possesses high conductivity caused by the formation of ordered graphitic carbon structure.^[11]

The porosity structures of Fe–N/MCHCS and N/MCHCS were confirmed by the nitrogen adsorption-desorption isotherms. Fe–N/MCHCS and N/MCHCS show type IV isotherm and type H₃ hysteresis loop (Figure 2c), indicating the existence of mesopores.^[12] Brunauer-Emmett-Teller (BET) surface area for Fe–N/MCHCS and N/MCHCS are $636\text{ m}^2\text{ g}^{-1}$ and $675\text{ m}^2\text{ g}^{-1}$, respectively. The similar BET surface area of Fe–N/MCHCS to N/MCHCS illustrates that the pore structure is well remained during modification of N/MCHCS by atomic Fe. The pore size distribution shows that Fe–N/MCHCS contains three sets of pores with

the diameter of 0.7 nm, 1.3 nm and 34.3 nm (Figure 2d). The micropore of 0.7 nm and 1.3 nm are generated by the evaporation of small molecular (such as, CO_2 , CO) during the pyrolysis of polymer. The mesopore around 34.3 nm is attributed to the multi-cavity structure, which is consistent with TEM image (Figure 1d). Fe–N/MCHCS displays the microporous volume of $0.17\text{ cm}^3\text{ g}^{-1}$ and large mesoporous volume of $1.17\text{ cm}^3\text{ g}^{-1}$ belonging to multiple cavities. Overall, Fe–N/MCHCS shows hierarchical porous structure and high pore volume, which can accommodate more amount of sulfur and the presence of multi cavities can buffer the volumetric expansion and electrode structure collapse after intercalation Li during the discharging process, and in the meantime enhance electronic contact.

The elemental state and chemical composition of Fe–N/MCHCS and N/MCHCS were investigated using X-ray photo-electron spectroscopy (XPS, Figures S3–S5). Only C, O and N elements are observed in N/MCHCS (Figure S2), while the Fe-2p peaks of XPS spectrum (Figure S4a) for Fe–N/MCHCS beside of C,

O and N appear around 720.5 eV and 711.9 eV, which are contributed to Fe 2p1/2 and Fe 2p3/2 of Fe^{3+} species.^[13] Inductively coupled plasma optical emission spectrometry (ICP-OES) analysis results show a Fe content of 0.17% in Fe–N/MCHCS. The XPS analysis of N species was shown in Figure S4(b), and the species of pyridinic (398.4 eV), graphitic (400.5 eV), and oxidized (401.4 eV) N are present in high-resolution N 1s spectrum with a nitrogen content of about 5.9%.^[14]

Electrocatalytic characterization of Fe–N/MCHCS

To evaluate the chemical adsorption ability of lithium polysulfides with Fe–N/MCHCS, a visualized adsorption test of polysulfides was conducted by soaking Fe–N/MCHCS (5 mg) into deep yellow Li_2S_4 solution. It was found that the solution with Fe–N/MCHCS was decolorized after static adsorption for 2 h (Figure 3a), suggesting excellent binding capability for liquid-phase polysulfides of the Fe–N/MCHCS. Significantly, the chemical adsorption is the precondition for the redox reaction of polysulfides on Fe–N/MCHCS electrocatalyst.^[15] The cyclic volt-

tammetry (CV) tests of the Li_2S_6 symmetric cells were first conducted to demonstrate the electrocatalytic property of Fe–N/MCHCS. As shown in Figure 3(b), Fe–N/MCHCS exhibits a higher polarization current density than that of N/MCHCS based cell, indicative of the enhanced catalytic reactivity of polysulfides liquid-liquid conversion kinetics (Li_2S_y to Li_2S_x , $8 \geq x > 2$, $8 \geq y > 2$) on the Fe–N/MCHCS electrocatalyst. Furthermore, the nucleation experiments of Li_2S were carried out to monitor the liquid-solid conversion kinetics on different surfaces. Apparently, the capacities of Li_2S precipitation on Fe–N/MCHCS (73 mAh g^{-1}) are higher than that of N/MCHCS (90 mAh g^{-1}) (Figure 3c), suggesting the promoted conversion efficiency for lithium polysulfides to Li_2S with Fe–N/MCHCS electrode. Besides, the reversible process of the dissolution solid Li_2S is also significantly improved by the Fe–N/MCHCS. After the fully conversion of sulfur to Li_2S , the Li_2S dissolution kinetics was evaluated by the potentiostatic charge process. An obvious oxidation peak of Li_2S dissolution at 1558 s is detected on Fe–N/MCHCS. In contrast, a delayed current signal is observed for N/MCHCS (3418 s) (Figure 3d). In addition, the sharply decreased impedance from N/MCHCS to Fe–N/MCHCS (from 68.6 to 64.7Ω) reflects the enhanced

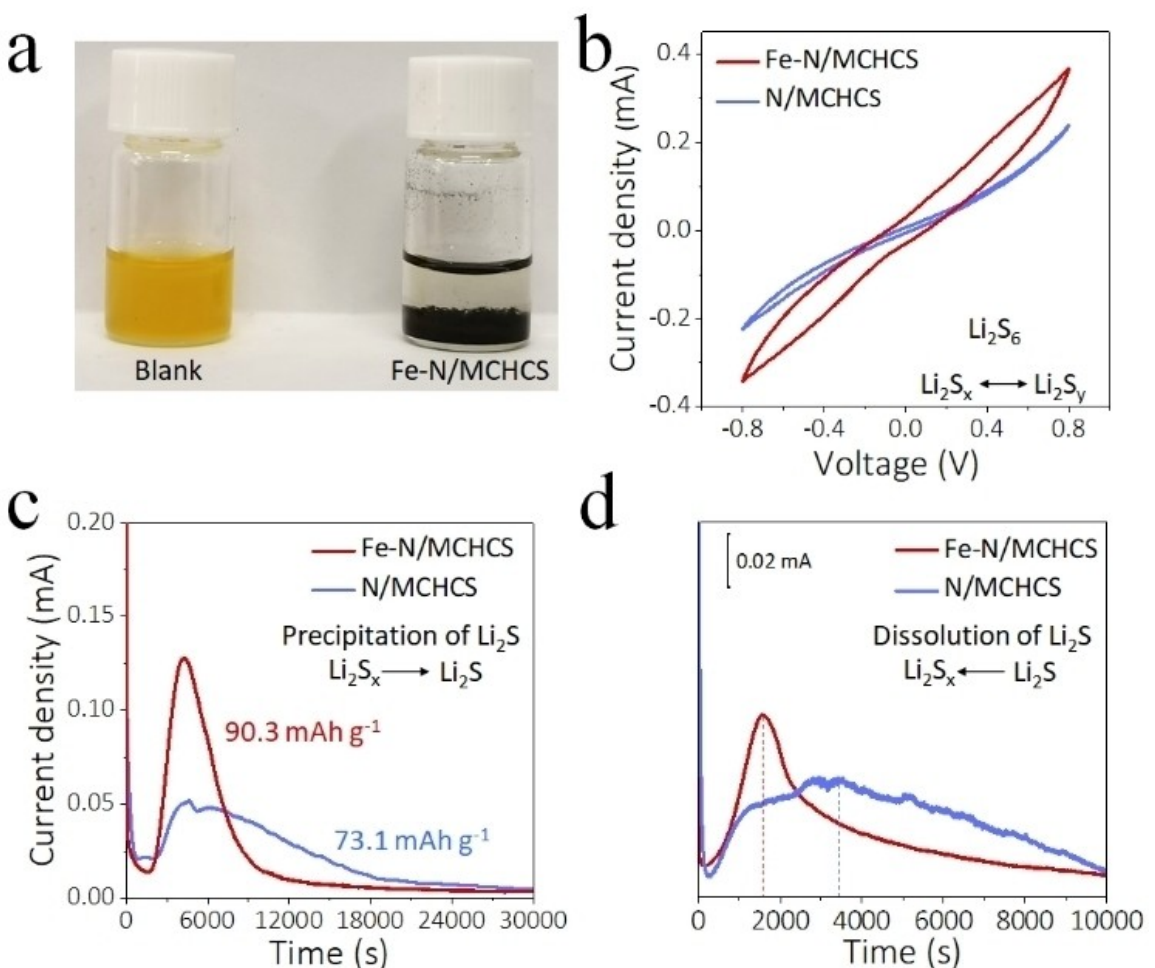


Figure 3. a) Variation in Li_2S_4 color upon adsorption by Fe–N/MCHCS. b) CV curves of Li_2S_6 symmetric cells using Fe–N/MCHCS and N/MCHCS obtained at 5 mV s^{-1} . c) Potentiostatic discharge profile at 2.05 V on Fe–N/MCHCS and N/MCHCS. d) Potentiostatic charge profile at 2.40 V for evaluating dissolution kinetic of Li_2S of Fe–N/MCHCS and N/MCHCS.

interface charge transfer (Figure S6), which indicates Fe–N/MCHCS is more favorable for electrochemical redox reactions of lithium polysulfides.

Electrochemical performance of Fe–N/MCHCS

To investigate the superiority of Fe–N/MCHCS for improving the electrochemical kinetics in working Li–S batteries, the Fe–N/MCHCS (Fe–N/MCHCS, Figure S7) cathode with a high sulfur mass loading of 85% was obtained by a melt-diffusion process. N/MCHCS–S with the same mass loading was also prepared for further comparison. Firstly, the CV curves were measured at a scan rate of 0.1 mV s^{-1} in a voltage range of 1.7–2.8 V. As shown in Figure 4(a), the initial three cycles of Fe–N/MCHCS–S cathode show no obvious current changes and peak shifts, indicating the excellent electrochemical reversibility and high-efficiency utilization of sulfur. Furthermore, Fe–N/MCHCS–S cathode shows the higher peak currents both in the cathodic and anodic processes than those of N/MCHCS–S cathode, implying that Fe–N/MCHCS behaves both as an oxidation and reduction catalyst for accelerating electron transfer to polysulfides (Figure S8). The excellent kinetics promotion of sulfur redox of Fe–N/MCHCS–S cathode guarantees their superior performance. Notably, a high capacity of 1423 mAh g^{-1} at 0.3 C ($1 \text{ C} = 1675 \text{ mA g}^{-1}$) is achieved for the Fe–N/MCHCS–S cathode. Under current density of 0.5, 1, 2, 3 and 5 C, a high discharge specific capacity of 1357, 1286, 1225, 1189 and 1113 mAh g^{-1} is maintained, respectively. Even when the rate is as high as 8 C, an unprecedented discharged specific capacity can still remain 1055 mAh g^{-1} . After high-rate cycling, switching the current density back to 0.5 C, an extremely high revisable capacity of 1341 mAh g^{-1} is recovered immediately, the coulombic efficiency remains at nearly 100%, suggesting that the conversion between S_8 and Li_2S_x is highly reversible. Additionally, the N/MCHCS–S cathode displays ineffective utiliza-

tion of sulfur with inferior rate performance, such as a lower discharge capacity of 1239 mAh g^{-1} at 0.3 C and a fast capacity fading to 874 mAh g^{-1} at 8 C along with unacceptable capacity recuperation after high-rate measurements (Figures 4b, S9 and 4c).

In addition, Fe–N/MCHCS–S based Li–S batteries also show significantly practical application potential with a high sulfur mass loading (5.0 mg cm^{-2}) and low electrolyte to sulfur ratio (E/S) of $8 \mu\text{L mg}^{-1}$, an excellent specific capacity of 965 mAh g^{-1} and corresponding areal capacity of 4.85 mAh cm^{-2} can be well achieved and maintained 984 mAh g^{-1} after 100 cycles (Figure 4d). Moreover, Fe–N/MCHCS–S electrode exhibits a high initial capacity of 1420 mAh g^{-1} and maintains 1135 mAh g^{-1} at 0.5 C with stabilized coulombic efficiency around 100% after 300 cycles (Figure 4e, f), corresponding to only 0.067% of capacity fading rate. In contrast, N/MCHCS–S delivers a lower initial capacity of 1342 mAh g^{-1} , and drastically drops to 812 mAh g^{-1} after 200 cycles with a fast average capacity fading of 0.197% each cycle (Figures 4f and S10). To identify structural superiority of multi-cavity hollow carbon spheres for trapping and promoting polysulfides, single-cavity hollow carbon spores (N/HCS) and atomic iron doped hollow carbon spores (Fe–N/HCS) with the diameter size of $\sim 200 \text{ nm}$ were also prepared (Figures S11 and S12). The BET surface area of Fe–N/HCS and N/HCS is only $175 \text{ m}^2 \text{ g}^{-1}$ and $180 \text{ m}^2 \text{ g}^{-1}$, respectively (Figure S13a, b), greatly lower than Fe–N/MCHCS ($636 \text{ m}^2 \text{ g}^{-1}$). The micropore diameter of Fe–N/HCS is 0.7 nm and 1.3 nm , which is the same as that of Fe–N/MCHCS due to the same pyrolysis process of both precursors, while the mesopore size distribution is very random (Figure S13c, d). What's more, compared with Fe–N/MCHCS, the microporous and mesoporous volume of $0.04 \text{ cm}^3 \text{ g}^{-1}$ and $0.63 \text{ cm}^3 \text{ g}^{-1}$ for Fe–N/HCS is much lower than Fe–N/MCHCS. As a consequence, a low initial discharge specific capacity of 1145 and 1104 mAh g^{-1} with a rapid capacity fade rate of 0.092% and 0.16% for Fe–N/HCS–S and N/HCS–S with the same

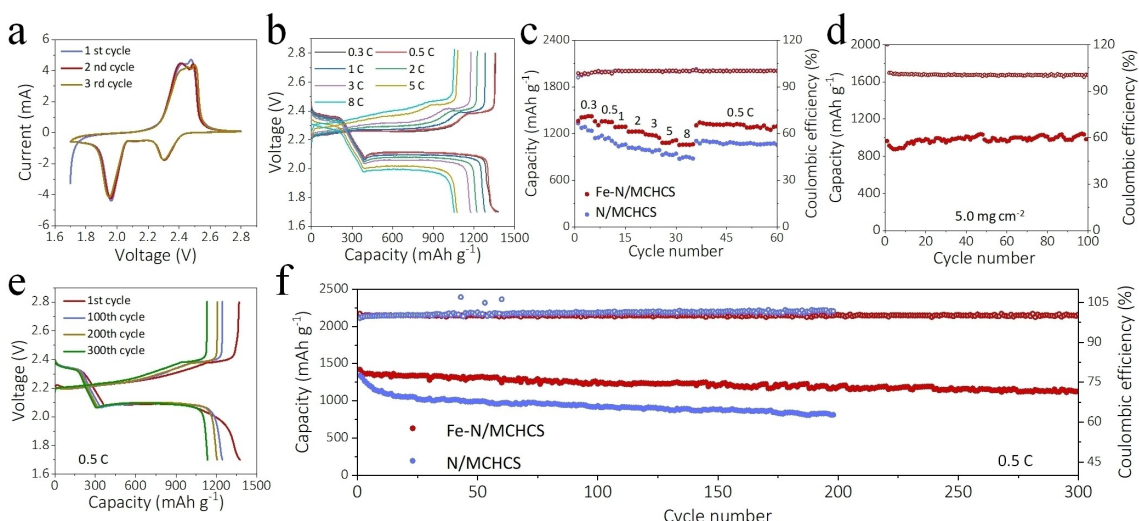


Figure 4. a) CV curves of Fe–N/MCHCS–S cathode for Li–S batteries. b) Galvanostatic charge/discharge profiles and c) capabilities of Fe–N/MCHCS–S and N/MCHCS–S at different rates. d) Cycling stability of Fe–N/MCHCS–S cathode for Li–S batteries at high sulfur loading of 5.0 mg cm^{-2} . e) Charge/discharge profiles of Li–S batteries based on Fe–N/MCHCS–S cathode at 0.5 C . f) Cycling stability of Fe–N/MCHCS–S and N/MCHCS–S Li–S batteries at 0.5 C over 300 cycles.

sulfur loading of 85% are displayed at 0.5 C (Figure S14). This can be attributed to the severe shuttle mitigation and sluggish sulfur redox chemistry kinetics of the sulfur hosts. Impressively, the superior lifetime of Fe–N/MCHCS–S based Li–S batteries was further tested at practical current density of 2 C, the discharge capacity is 1059 mAh g⁻¹ with an average decay rate per cycle of only 0.042% during 300 cycles due to the structural and chemical advantages of the Fe–N/MCHCS composites (Figures S15 and S16). In addition, the efficient formation of solid Li₂S from long chained S₈ during discharge process and vice versa were verified by the in-situ XRD patterns (Figure S17).^[16] Notably, the valid restriction of polysulfides in Fe–N/MCHCS could inhibit lithium dendrite growth and efficiently avoid the Li metal anode from the damage of polysulfides, which was further confirmed by the Li anode from SEM images of disassembling Fe–N/MCHCS–S based batteries after 50 cycles at 2 C (Figure S18), observing only a minor lithium anode corrosion.

Conclusion

In summary, we have developed a novel physically/chemically double-confined catalytic nanoreactor of Fe–N/MCHCS for Li–S batteries to anchor polysulfides and synchronously promote the redox kinetics between polysulfides and solid Li₂S. The Fe–N/MCHCS hosts integrating large surface area and high pore volume allow the high content of sulfur, and multi-cavity structure guarantees continuous and expedite electron transfer. More importantly, the uniform dispersed atomic Fe–N sites enhance the chemical bonding and show high electrocatalytic activities to facilitate the redox reaction dynamics of polysulfides. When used in Li–S batteries, the Fe–N/MCHCS–S cathode shows stable capacity retention and a low capacity decay rate of per cycle 0.042% over 300 cycles, high columbic efficiency of 100% and significantly enhanced rate performance of 1055 mAh g⁻¹ at 8 C. Additionally, the Fe–N/MCHCS–S cathode can realize an areal capacity of 4.85 mAh cm⁻² at 5.0 mg cm⁻². Overall, our work suggests the great opportunity of atomic Fe and N co-doped carbon sphere nanoreactor as an effective sulfur host for high performance Li–S batteries.

Experimental Section

Synthesis of N/MCHCS

First, the templates of SiO₂ spheres and HMSS were synthesized.^[17] Second, 0.1 g HMSS as template was dispersed in the mixture of H₂O (18 mL), ethanol (47 mL) and ammonia (1 mL) and stirred for 30 min. Then, 0.25 g dopamine hydrochloride was dissolved in the mixture of 3 mL H₂O and 2 mL ethanol and added into the above mixture containing HMCC. After stirring for 24 h, the solid particles were separated by centrifuge and dried at 100°C in an oven. The synthesized solid was carbonized at 800°C for 2 h in N₂ atmosphere. Finally, the HMSS template in the synthesized powder was etched by HF and N/MCHCS was obtained. For comparison, N/HCS was synthesized using the same procedure with that for N/MCHCS except the template from HMSS to solid SiO₂ spheres.

Synthesis of Fe–N/MCHCS and Fe–N/HCS

The Fe atoms were anchored on N/MCHCS or N/HCS via the coordination interaction with nitrogen species. Specially, N/MCHCS or N/HCS (20 mg) was dispersed into 10 mL dimethyl formamide (DMF) containing 8.24 mg Fe(acac)₃ under sonication for 1 h, and then heated at 80°C for 5 h under constant stirring. Subsequently, DMF solvent was removed by the vacuum rotary evaporation and the obtained solid was pyrolyzed at 700°C for 2 h under nitrogen atmosphere, followed by the acid washing with 0.1 M HCl at 80°C for 5 h. Finally, the solid was separated via vacuum filtration and dried at 60°C in a vacuum oven. The obtained solids were denoted as Fe–N/MCHCS and Fe–N/HCS, respectively.

Synthesis of sulfur composite electrode

The sulfur composite was prepared via the facile diffusion method.^[18] The sulfur and sample powder (N/MCHCS, N/HCS, Fe–N/MCHCS and Fe–N/HCS) with designed weight ratio were uniformly grinded. Then, the obtained mixtures were pressed and annealed at 155°C for 24 h under Ar atmosphere to obtain the sulfur composite.

Measurement for Li₂S nucleation and Li₂S dissolution

The nucleation and dissolution of Li₂S were studied by potentiostatic deposition and decomposition of Li₂S₈ catholyte (0.15 mol L⁻¹) on Fe–N/MCHCS and N/MCHCS surface. For the Li₂S nucleation test, the cells were galvanostatically discharged at a constant current density of 0.112 mA to 2.06 V and then keep voltage at 2.05 V for Li₂S growth until the current dropped below 10⁻⁵ A. The capacities of the deposition of Li₂S were evaluated according to Faraday's law.^[19] For the Li₂S dissolution, firstly, the cells were galvanostatically discharged at a constant of 0.10 mA to 1.80 V, and then galvanostatically discharged to 1.80 V at 0.01 mA to ensure the sufficient transformation of Li₂S on the sample surface. Afterward, the cells were potentiostatically charged at 2.40 V until the charge current was below 10⁻⁵ A.

Electrochemical measurement

Fe–N/MCHCS–S (or N/MCHCS–S, N/HCS–S, Fe–N/HCS–S), conductive carbon black and binder polyvinylidene fluoride (PVDF) with a mass ratio of 8:1:1. 1.0 M solution of LiTFSI with 1 wt% LiNO₃ in 1,3-dioxolane (DOL) and 1,2-dimethoxyethane (DME) was used as the electrolyte. The cathode was punched into disks with a diameter of 12 mm, polypropylene (PP) membrane (Celgard 2400) was used as the separator. The average mass of sulfur was controlled around 1.0 mg cm⁻² and the E/S was around 10. The catalytic performances Fe–N/MCHCS and N/MCHCS were studied by CV measurement of the symmetric cell at a scan rate of 10 mV s⁻¹ between -0.8 and 0.8 V with Li₂S₆ (0.2 mol L⁻¹) catholyte. The performances of Li–S batteries were measured on a Neware battery analyzer (CT-4008Q, Shenzhen, China) under different current rates at a voltage interval from 1.7 to 2.8 V. The CV curves were carried out on a CHI-760E electrochemical workstation (Chenhua Instrument, Shanghai) at a scan rate of 0.1 mV s⁻¹. Electrochemical impedance spectroscopy was measured in the scan frequency range of 100 kHz–10 mHz.

Analytical techniques

The morphology of Fe–N/MCHCS and N/MCHCS etc. was observed using TEM (HITACHI HT7700) at an acceleration voltage of 100 kV and SEM (FEI QUANTA 200F) at an acceleration voltage of 20 kV. The HAADF-STEM measurements were performed with JEM-ARM200F. N₂ adsorption-desorption isotherms were obtained at 77 K on a Micro-

meritics Tristar II 3020 automated analyzer. The surface areas were estimated according to the BET method. The XRD pattern was performed on Rigaku D/Max2500PC diffractometer ($\text{Cu } K_{\alpha}, \lambda = 1.5418 \text{ \AA}$) at a scanning speed of $5^\circ/\text{min}$ at room temperature. XPS analysis was conducted via the VG ESCALAB MK2 apparatus using $\text{Al } K_{\alpha}$ as the excitation light source.

Acknowledgements

H.D. Shi and P.P. Su contributed equally to this work. This work was financially supported by the National Natural Science Foundation of China (Grant Nos. 22125903, 51872283, 21905271), Dalian Innovation Support Plan for High Level Talents (2019RT09), Dalian National Laboratory For Clean Energy (DNL), CAS, DNL Cooperation Fund, CAS (DNL201912, DNL201915, DNL202016, DNL202019), DICP (DICP ZZBS201802, DICP I2020032), the Joint Fund of the Yulin University and the Dalian National Laboratory for Clean Energy (YLU-DNL Fund 2021002, YLU-DNL Fund 2021009).

Conflict of Interest

The authors declare no conflict of interest.

Data Availability Statement

The data that support the findings of this study are available from the corresponding author upon reasonable request.

Keywords: atomic Fe doping · hollow carbon · lithium-sulfur battery · multi-cavity · nanoreactor

- [1] a) J. Kim, D. J. Lee, H. G. Jung, Y. K. Sun, J. Hassoun, B. Scrosati, *Adv. Funct. Mater.* **2013**, *23*, 1076–1080; b) Y. X. Yin, S. Xin, Y. G. Guo, L. J. Wan, *Angew. Chem. Int. Ed.* **2013**, *52*, 13186–13200; *Angew. Chem.* **2013**, *125*, 13426–13441; c) R. Fang, S. Zhao, Z. Sun, D. W. Wang, H. M. Cheng, F. Li, *Adv. Mater.* **2017**, *29*, 1606823; d) M. Wild, L. O’neill, T. Zhang, R. Purkayastha, G. Minton, M. Marinescu, G. Offer, *Energy Environ. Sci.* **2015**, *8*, 3477–3494.
- [2] a) Y. Boyjoo, H. Shi, Q. Tian, S. Liu, J. Liang, Z.-S. Wu, M. Jaroniec, J. Liu, *Energy Environ. Sci.* **2021**, *14*, 540–575; b) T. Liu, H. Hu, X. Ding, H. Yuan, C. Jin, J. Nai, Y. Liu, Y. Wang, Y. Wan, X. Tao, *Energy Storage Mater.* **2020**, *30*, 346–366; c) L. Ma, K. E. Hendrickson, S. Wei, L. A. Archer, *Nano Today* **2015**, *10*, 315–338.
- [3] a) S.-E. Cheon, K.-S. Ko, J.-H. Cho, S.-W. Kim, E.-Y. Chin, H.-T. Kim, *J. Electrochem. Soc.* **2003**, *150*, A796; b) L. Qie, C. Zu, A. Manthiram, *Adv. Energy Mater.* **2016**, *6*, 1502459; c) H. Shi, X. Zhao, Z.-S. Wu, Y. Dong, P. Lu, J. Chen, W. Ren, H.-M. Cheng, X. Bao, *Nano Energy* **2019**, *60*, 743–751.
- [4] a) A. Manthiram, Y. Fu, Y.-S. Su, *Acc. Chem. Res.* **2013**, *46*, 1125–1134; b) J. Guo, Y. Xu, C. Wang, *Nano Lett.* **2011**, *11*, 4288–4294; c) Y. Boyjoo, H. Shi, E. Olsson, Q. Cai, Z. S. Wu, J. Liu, G. Q. Lu, *Adv. Energy Mater.* **2020**, *10*, 2000651.
- [5] a) Q. Zhang, X. Cheng, J. Huang, H. Peng, F. Wei, *Carbon* **2015**, *81*, 850; b) L. Borchardt, M. Oschatz, S. Kaskel, *Chem. Eur. J.* **2016**, *22*, 7324–7351; c) M. Yu, R. Li, M. Wu, G. Shi, *Energy Storage Mater.* **2015**, *1*, 51–73.

- [6] a) X. Li, Y. Cao, W. Qi, L. V. Saraf, J. Xiao, Z. Nie, J. Mietek, J.-G. Zhang, B. Schwenzer, J. Liu, *J. Mater. Chem.* **2011**, *21*, 16603–16610; b) A. Fu, C. Wang, F. Pei, J. Cui, X. Fang, N. Zheng, *Small* **2019**, *15*, 1804786; c) Z.-L. Xu, J.-K. Kim, K. Kang, *Nano Today* **2018**, *19*, 84–107; d) G. He, S. Evers, X. Liang, M. Cuisinier, A. Garsuch, L. F. Nazar, *ACS Nano* **2013**, *7*, 10920–10930.
- [7] a) Z. Li, L. Yuan, Z. Yi, Y. Sun, Y. Liu, Y. Jiang, Y. Shen, Y. Xin, Z. Zhang, Y. Huang, *Adv. Energy Mater.* **2014**, *4*, 1301473; b) M. Wang, X. Xia, Y. Zhong, J. Wu, R. Xu, Z. Yao, D. Wang, W. Tang, X. Wang, J. Tu, *Chem. Eur. J.* **2019**, *25*, 3710–3725; c) H. Tian, J. Liang, J. Liu, *Adv. Mater.* **2019**, *31*, 1903886.
- [8] a) C. Zhang, H. B. Wu, C. Yuan, Z. Guo, X. W. Lou, *Angew. Chem. Int. Ed.* **2012**, *51*, 9592–9595; *Angew. Chem.* **2012**, *124*, 9730–9733; b) T. Liu, L. Zhang, B. Cheng, J. Yu, *Adv. Energy Mater.* **2019**, *9*, 1803900; c) Q. Sun, B. He, X.-Q. Zhang, A.-H. Lu, *ACS Nano* **2015**, *9*, 8504–8513.
- [9] a) H. Yuan, X. Chen, G. Zhou, W. Zhang, J. Luo, H. Huang, Y. Gan, C. Liang, Y. Xia, J. Zhang, *ACS Energy Lett.* **2017**, *2*, 1711–1719; b) Z. Sun, J. Zhang, L. Yin, G. Hu, R. Fang, H.-M. Cheng, F. Li, *Nat. Commun.* **2017**, *8*, 1–8; c) X. Liu, J. Q. Huang, Q. Zhang, L. Mai, *Adv. Mater.* **2017**, *29*, 1601759; d) D. Liu, C. Zhang, G. Zhou, W. Lv, G. Ling, L. Zhi, Q. H. Yang, *Adv. Sci.* **2018**, *5*, 1700270; e) H. Wang, W. Zhang, J. Xu, Z. Guo, *Adv. Funct. Mater.* **2018**, *28*, 1707520; f) M. Zhao, B.-Q. Li, X.-Q. Zhang, J.-Q. Huang, Q. Zhang, *ACS Cent. Sci.* **2020**, *6*, 1095–1104; g) X. Liang, C. Y. Kwok, F. Lodi-Marzano, Q. Pang, M. Cuisinier, H. Huang, C. J. Hart, D. Houtarde, K. Kaup, H. Sommer, *Adv. Energy Mater.* **2016**, *6*, 1501636.
- [10] a) Z. Zhuang, Q. Kang, D. Wang, Y. Li, *Nano Res.* **2020**, *13*, 1856–1866; b) H. Shi, X. Ren, J. Lu, C. Dong, J. Liu, Q. Yang, J. Chen, Z. S. Wu, *Adv. Energy Mater.* **2020**, *10*, 2002271; c) Z. Du, X. Chen, W. Hu, C. Chuang, S. Xie, A. Hu, W. Yan, X. Kong, X. Wu, H. Ji, *J. Am. Chem. Soc.* **2019**, *141*, 3977–3985; d) C. Lu, R. Fang, X. Chen, *Adv. Mater.* **2020**, *32*, 1906548; e) G. Zhou, S. Zhao, T. Wang, S.-Z. Yang, B. Johannessen, H. Chen, C. Liu, Y. Ye, Y. Wu, Y. Peng, C. Liu, S. P. Jiang, Q. Zhang, Y. Cui, *Nano Lett.* **2020**, *20*, 1252–1261; f) T. Huang, Y. Sun, J. Wu, J. Jin, C. Wei, Z. Shi, M. Wang, J. Cai, X.-T. An, P. Wang, C. Su, Y.-Y. Li, J. Sun, *ACS Nano* **2021**, *15*, 14105–14115; g) S. Zhang, X. Ao, J. Huang, B. Wei, Y. Zhai, D. Zhai, W. Deng, C. Su, D. Wang, Y. Li, *Nano Lett.* **2021**, *21*, 9691–9698; h) R. Xiao, K. Chen, X. Zhang, Z. Yang, G. Hu, Z. Sun, H.-M. Cheng, F. Li, *J. Energy Chem.* **2021**, *54*, 452–466.
- [11] a) M. S. Dresselhaus, G. Dresselhaus, R. Saito, A. Jorio, *Phys. Rep.* **2005**, *409*, 47–99; b) Y. Wang, D. C. Alsmeyer, R. L. McCreery, *Chem. Mater.* **1990**, *2*, 557–563.
- [12] a) G. Xu, J. Han, B. Ding, P. Nie, J. Pan, H. Dou, H. Li, X. Zhang, *Green Chem.* **2015**, *17*, 1668–1674; b) M. Oschatz, S. Thieme, L. Borchardt, M. R. Lohe, T. Biemelt, J. Brückner, H. Althues, S. Kaskel, *Chem. Commun.* **2013**, *49*, 5832–5834.
- [13] a) J. Han, X. Meng, L. Lu, J. Bian, Z. Li, C. Sun, *Adv. Funct. Mater.* **2019**, *29*, 1808872; b) C. Zhu, S. Fu, J. Song, Q. Shi, D. Su, M. H. Engelhard, X. Li, D. Xiao, D. Li, L. Estevez, *Small* **2017**, *13*, 1603407.
- [14] a) M. Xiao, J. Zhu, L. Ma, Z. Jin, J. Ge, X. Deng, Y. Hou, Q. He, J. Li, Q. Jia, *ACS Catal.* **2018**, *8*, 2824–2832; b) W. Wang, X. Zuo, Q. Yang, Q. Yang, H. Tang, H. Zhang, G. Li, *Appl. Catal. B* **2021**, 120726.
- [15] a) Y. Wang, L. Zhou, J. Huang, X. Wang, X. Xu, J. Lu, Y. Tian, Z. Ye, H. Tang, S. T. Lee, *Adv. Funct. Mater.* **2020**, *30*, 1910331; b) Z. Cheng, H. Pan, J. Chen, X. Meng, R. Wang, *Adv. Energy Mater.* **2019**, *9*, 1901609.
- [16] H. Shi, J. Qin, P. Lu, C. Dong, J. He, X. Chou, P. Das, J. Wang, L. Zhang, Z. S. Wu, *Adv. Funct. Mater.* **2021**, *31*, 2102314.
- [17] L. Yin, Q. Tian, Y. Boyjoo, G. Hou, X. Shi, J. Liu, *Langmuir* **2019**, *36*, 6984–6993.
- [18] T. Boenke, P. Härtel, S. Dörfler, T. Abendroth, F. Schwotzer, H. Althues, S. Kaskel, *Batteries & Supercaps* **2021**, *4*, 989–1002.
- [19] Y.-Q. Peng, M. Zhao, Z.-X. Chen, Q. Cheng, Y. Liu, C.-X. Zhao, X. Ma, B.-Q. Li, C.-M. Chen, J.-Q. Huang, Q. Zhang, *Batteries & Supercaps* **2022**, *5*, e202100359.

Manuscript received: April 1, 2022

Revised manuscript received: April 21, 2022

Accepted manuscript online: April 22, 2022

Version of record online: May 9, 2022